Available online at www.sciencedirect.com
ScienceDirect
Composites Science and Technology 68 (2008) 354–366
COMPOSITES SCIENCE AND TECHNOLOGY
www.elsevier.com/locate/compscitech

Static and free vibration analysis of laminated composite plates using the conforming radial point interpolation method

G.R. Liu [a,b], X. Zhao [a,*], K.Y. Dai [a], Z.H. Zhong [c], G.Y. Li [c], X. Han [c]

[a] Centre for Advanced Computations in Engineering Science (ACES), Department of Mechanical Engineering, The National University of Singapore, 9 Engineering Drive 1, Singapore 117576, Singapore
[b] The Singapore-MIT Alliance (SMA), E4-04-10, 4 Engineering Drive 3, Singapore 117576, Singapore
[c] Key Laboratory of Advanced Technology for Vehicle Body Design and Manufacture, M.O.E, Hunan University, Changsha 410082, People's Republic of China

Received 4 September 2006; received in revised form 24 May 2007; accepted 3 July 2007
Available online 2 August 2007

Abstract

In this paper, a mesh-free formulation for the static and free vibration analyses of composite plates is presented via a linearly conforming radial point interpolation method. The radial and polynomial basis functions are employed to construct the shape functions bearing Delta function property. A strain smoothing stabilization technique for nodal integration is employed to restore the conformability and to improve the accuracy and the rate of convergence. The present formulation is based on the first order shear deformation plate theory, with effective treatment for shear-locking and hence is applicable for both thin and relatively thick plates. To verify the accuracy and stability of the present formulation, intensive comparisons are made with existing results available in the literature and good agreements are obtained. The numerical examples have confirmed the significant features of the present method: (1) very stable and accurate for extremely distributed nodes; (2) shear-locking can be avoid very easily in the present formulation; (3) applicable for problems of complex domains.

Keywords: A. Composite plates; C. Mesh-free; C. Point interpolation; C. Radial basis function; C. Nodal integration

1. Introduction

The static and vibration analyses of plates have been studied extensively by researchers using various numerical methods. The development of numerical approaches has led the invention of some important methods, including Ritz method, finite difference method (FDM), finite element method (FEM), etc. Although these methods have demonstrated efficiency and accuracy in solving plate problems, there are still some limitations in engineering applications. In Ritz method, it is difficult to choose the appropriate trial functions for complicated problems; the FDM is more flexible than the Ritz method, but requires a set of "structured" grids, which limits its application for problems of complex geometry. The FEM is so far the most flexible and effective for complicated geometry, but there are problems related to meshing and mesh distortion. A promising numerical technique, mesh-free method, developed in recent years (see, e.g., [1,2]), has shown some superiorities over traditional numerical methods.

Since the first weak form mesh-free method, the diffuse element method (DEM), was proposed by Nayroles et al. [3], various mesh-free methods have been developed. Such as element-free Galerkin (EFG) method [4], smooth particle hydrodynamic (SPH) method [5,6], reproducing kernel particle method (RKPM) [7], Petrov–Galerkin mesh-free [8], corrective smoothed particle method (CSPM) [9], modified smoothed-particle hydrodynamics (MSPH) [10] and point interpolation methods (PIM) [11–13]. In the weak form mesh-free methods, a background mesh or a background cell structure is commonly used to compute the

* Corresponding author. Tel.: +65 6516 4797; fax: +65 6516 4795.
E-mail address: mpezx@nus.edu.sg (X. Zhao).

0266-3538/$ - see front matter © 2007 Elsevier Ltd. All rights reserved.
doi:10.1016/j.compscitech.2007.07.014

integrals. Recently, the nodal integration techniques have been developed by performing the integrals based on nodes. Beissel and Belytschko [14] demonstrated that the nodal integration of EFG resulted in a spatial instability due to the under integration of the weak form. They proposed a stabilized procedure to eliminate the spatial instability. Bonet and Kulasegaram [15] presented a least-square stabilization technique to eliminate spurious mode in nodal integration. A stabilized conforming nodal integration approach for Galerkin mesh-free methods has been proposed by Chen et al. [16] to eradicate spatial instability in nodal integration. An integration constraint (IC) was introduced as a necessary condition for a linear exactness in mesh-free Galerkin approximation. It has been revealed that the Gauss integration violates the integration constraint (IC) and leads to noticeable error for linear solutions. A strain smoothing stabilization procedure was proposed to compute the nodal strain by applying a divergence theorem. A mesh-free Mindlin–Reissner plate formulation was provided by Wang and Chen [17] using the stabilized conforming nodal integration to remove the shear-locking phenomena.

For the analysis of laminated plates, some analytical solutions have been reported by Srinivas and Rao [18], Srinivas et al. [19], Pagano [20] and Vel and Batra [21]. For some complicated cases where analytical solutions are difficult to obtain, however, numerical methods are usually adopted to attain the approximation results, such as meshless local Petrov–Galerkin method (MLPG) by Qian et al. [22] and collocation method by Firreira et al. [23]. Radial basis functions (RBFs), which are widely used in the mathematics community for function fitting and solving PDEs using global nodes and collocation procedures [24,25], have been employed for the construction of shape functions in numerical methods. Some applications of RBFs in composite plates analysis have been presented by Ferreira and co-workers [26–29], and Xiao et al. [30].

The radial point interpolation meshless method (RPIM) [12,31] has been demonstrated to be an efficient meshless method and successfully applied in many engineering problems [32–36]. Both radial basis and polynomial functions are employed to construct the shape functions. The interpolation approximation passes through all scattered nodes in an influence domain, hence, the shape functions possess the delta function properties, which make the essential boundary conditions be imposed directly. Moreover, the moment matrix can be always inverted due to the employment of radial basis function. In this paper, a formulation for static and free vibration analyses of composite plates is provided using radial point interpolation meshless method (RPIM), where a stabilized conforming nodal integration instead of Gauss integration is adopted to evaluate the stiffness matrix. The present solution is based on the first order shear deformation plate theory that is a general form of the Mindlin–Reissner plate theory and Galerkin weak form formulation. To validate the accuracy and stability of the present method, an intensive study has been carried out for different node distributions, and comparisons were made with results available in literature. The static deflections and free vibration of plates with different shapes and boundary conditions are also examined.

2. Shape function construction

Consider an approximation function $u(\mathbf{x})$ in a domain Ω, which has a set of arbitrarily distributed points $\mathbf{x}_i$, $(i = 1,2,\ldots,\mathrm{NP})$, NP is the total number of nodes in the domain. It is assumed that, for a certain point x_k, only the nodes in a local sub-domain around x_k, for example, n nodes altogether, determine the value of $u(x_k)$. The effect of the nodes outside the sub-domain is neglected. This sun-domain is called influence domain or support domain. The radius of the influence domain is expressed by the product of a scaling factor and the maximum distance among neighboring nodes in the influence domain [27]. Therefore, the approximation of function $u(\mathbf{x})$ can be expressed as

$$u(\mathbf{x}) = \sum_{i=1}^{n} r_i(\mathbf{x})a_i + \sum_{j=1}^{m} p_j(\mathbf{x})b_j = \mathbf{r}^{\mathrm{T}}(\mathbf{x})\mathbf{a} + \mathbf{p}^{\mathrm{T}}(\mathbf{x})\mathbf{b} \tag{1}$$

where a_i is the coefficient for the radial basis function $r_i(\mathbf{x})$ and b_j the coefficient for polynomial basis $p_j(\mathbf{x})$, m is determined according to the polynomial basis selected. For example, a quadratic basis requires $m = 6$. The radial basis function $r_i(\mathbf{x})$ for two dimensional problems are defined as

$$r_i(x,y) = [(x-x_i)^2 + (y-y_i)^2 + R_c^2]^q \tag{2}$$

where q and R_c are two shape parameters, which are real and had been examined in detail by Wang and Liu [27]. A quadratic polynomial basis function $p_j(\mathbf{x})$ is given by

$$\mathbf{p}^{\mathrm{T}}(\mathbf{x}) = [1, x, y, x^2, xy, y^2] \tag{3}$$

The coefficients a_i and b_j in Eq. (1) are determined by satisfying the reproducing condition over the influence domain. The interpolation at the kth node is expressed as

$$u_k = u(\mathbf{x}_k) = \sum_{i=1}^{n} a_i r_i(\mathbf{x}_k) + \sum_{j=1}^{m} b_j p_j(\mathbf{x}_k) \tag{4}$$

In order to solve coefficients a_i and b_j, the following constraints are imposed

$$\sum_{i=1}^{n} p_j(\mathbf{x}_k)a_i = 0, \quad j = 1,2,\ldots,m \tag{5}$$

Eqs. (4) and (5) can be expressed in matrix form as

$$\begin{bmatrix} \mathbf{r}_0 & \mathbf{p}_0 \\ \mathbf{p}_0^{\mathrm{T}} & \mathbf{0} \end{bmatrix} \begin{Bmatrix} \mathbf{a} \\ \mathbf{b} \end{Bmatrix} = \begin{Bmatrix} \mathbf{u}^e \\ \mathbf{0} \end{Bmatrix} \quad \text{or} \quad \mathbf{G}\begin{Bmatrix} \mathbf{a} \\ \mathbf{b} \end{Bmatrix} = \begin{Bmatrix} \mathbf{u}^e \\ \mathbf{0} \end{Bmatrix} \tag{6}$$

where nodal displacement vector $\mathbf{u}^e$ is given by

$$\mathbf{u}^e = [u_1, u_2, u_3, \ldots, u_n]^{\mathrm{T}} \tag{7}$$

The coefficient matrix $\mathbf{r}_0$ is expressed as

$$\mathbf{r}_0 = \begin{bmatrix} r_1(x_1,y_1) & r_2(x_1,y_1) & \cdots & r_n(x_1,y_1) \\ r_1(x_2,y_2) & r_2(x_2,y_2) & \cdots & r_n(x_2,y_2) \\ \vdots & \vdots & \vdots & \vdots \\ r_1(x_n,y_n) & r_2(x_n,y_n) & \cdots & r_n(x_n,y_n) \end{bmatrix} \tag{8}$$

The coefficient matrix $\mathbf{p}_0$ is defined as

$$\mathbf{p}_0 = \begin{bmatrix} p_1(x_1,y_1) & p_2(x_1,y_1) & \cdots & p_m(x_1,y_1) \\ p_1(x_2,y_2) & p_2(x_2,y_2) & \cdots & p_m(x_2,y_2) \\ \vdots & \vdots & \vdots & \vdots \\ p_1(x_n,y_n) & p_2(x_n,y_n) & \cdots & p_m(x_n,y_n) \end{bmatrix} \tag{9}$$

Eq. (6) can be solved for coefficients a_i and b_j

$$\begin{Bmatrix} \mathbf{a} \\ \mathbf{b} \end{Bmatrix} = \mathbf{G}^{-1} \begin{Bmatrix} \mathbf{u}^e \\ \mathbf{0} \end{Bmatrix} \tag{10}$$

The approximation of function $u(\mathbf{x})$ is finally expressed as

$$u(\mathbf{x}) = \begin{bmatrix} \mathbf{r}^{\mathrm{T}}(\mathbf{x}) & \mathbf{p}^{\mathrm{T}}(\mathbf{x}) \end{bmatrix} \mathbf{G}^{-1} \begin{Bmatrix} \mathbf{u}^e \\ \mathbf{0} \end{Bmatrix} = \varphi(\mathbf{x})\mathbf{u}^e \tag{11}$$

where $\varphi(\mathbf{x})$ is the matrix of the shape functions and given by

$$\varphi(\mathbf{x}) = [\phi_1(\mathbf{x}), \phi_2(\mathbf{x}), \ldots, \phi_n(\mathbf{x})] \tag{12}$$

The present shape functions possess the reproducing property due to the addition of polynomial basis, also satisfy the Delta function properties and partition of unity, and always exist because of the adoption of RBFs (see, e.g., [1]).

3. Strain smoothing technique

For linear exactness in Galerkin approximation, it has been demonstrated by Chen et al. [16] that the employment of linearly consistent shape functions does not guarantee a linear exactness in the solution, integration constraints (IC) need to be satisfied in domain integration. A detailed investigation on integration constraints has been carried out by Chen et al. [16]. They proposed a strain smoothing method in order to remove the instability in nodal integration. The strain smoothing technique is incorporated in present RPIM method for plate analysis, and briefly described as below:

For a two dimensional domain Ω, the strain smoothing at a node is given by

$$\tilde{\varepsilon}_{ij}(\mathbf{x}_L) = \frac{1}{A_L} \int_{\Omega} \varepsilon_{ij}(\mathbf{x})\, \mathrm{d}\Omega \tag{13}$$

where $A_L = \int_{\Omega_L} \mathrm{d}\Omega$ is the area of the representative domain of node L, as shown in Fig. 1, which can be obtained either from the Voronoi diagram or Delaunay triangulation. By employing the divergence theorem to Eq. (13), the following strain smoothing expression is obtained

$$\tilde{\varepsilon}_{ij}(x_L) = \frac{1}{2A_L} \int_{\Gamma_L} (u_i n_j + u_j n_i)\, \mathrm{d}\Gamma \tag{14}$$

where Γ_L is the boundary of the representative domain of node L, $\mathbf{n}$ is the surface normal on Γ_L, as shown in Fig. 1. Introducing RPIM shape functions into Eq. (14) yields

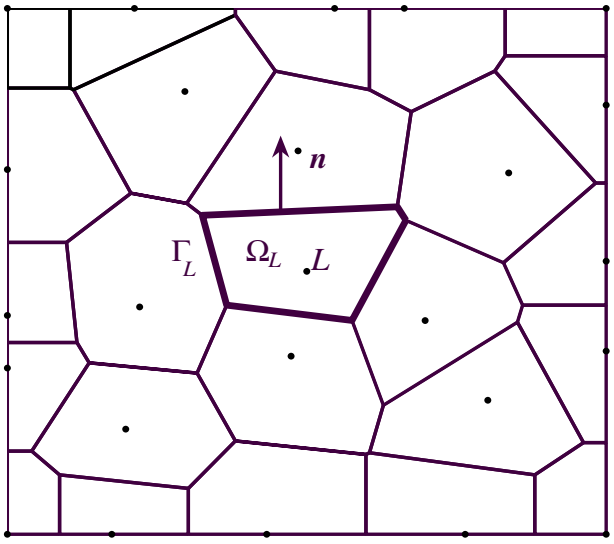

Fig. 1. Geometry of a representative node domain and its Voronoi domain.

$$\tilde{\boldsymbol{\varepsilon}}^h(x_L) = \sum_{I \in S_L} \tilde{\mathbf{B}}_{\mathrm{I}}(\mathbf{x}_L)\mathbf{u}_{\mathrm{I}} \tag{15}$$

$$\tilde{\mathbf{B}}_{\mathrm{I}}(\mathbf{x}_L) = \begin{bmatrix} \tilde{\nabla}_1\phi_{\mathrm{I}}(\mathbf{x}_L) & 0 \\ 0 & \tilde{\nabla}_2\phi_{\mathrm{I}}(\mathbf{x}_L) \\ \tilde{\nabla}_2\phi_{\mathrm{I}}(\mathbf{x}_L) & \tilde{\nabla}_1\phi_{\mathrm{I}}(\mathbf{x}_L) \end{bmatrix} \tag{16}$$

$$\tilde{\nabla}_i\phi_{\mathrm{I}}(\mathbf{x}_L) = \frac{1}{A_L} \int_{\Gamma_L} \phi_{\mathrm{I}}(\mathbf{x}_L) n_i(\mathbf{x}_L)\, \mathrm{d}\Gamma \tag{17}$$

where S_L is a group of nodes in the corresponding shape function supports for node L. To ensure the accuracy and convergence in applying the smoothed strain for stabilization in the nodal integration, the integration constraints require being satisfied. It has been demonstrated that the smoothing gradient equation (17) satisfies the integration constraints when reproducing kernel shape functions are introduced [16]. Due to the reproducing properties of RPIM shape functions, it is concluded that the integration constraints still hold when the present RPIM shape functions are employed.

4. Formulation

4.1. Energy functional for plates

Consider a plate with thickness h, as shown in Fig. 2, where a coordinate system (x,y,z) is fixed on the middle plane of the plate. According to the first order shear deformation theory, the displacement field is expressed as

$$\begin{aligned} u(x,y,z) &= u_0(x,y) - z\theta_x(x,y) \\ v(x,y,z) &= v_0(x,y) - z\theta_y(x,y) \\ w(x,y,z) &= w_0(x,y) \end{aligned} \tag{18}$$

where u_0, v_0 and w_0 denote the displacements of the mid-plane of the plate in the x, y, and z directions, θ_x and θ_y

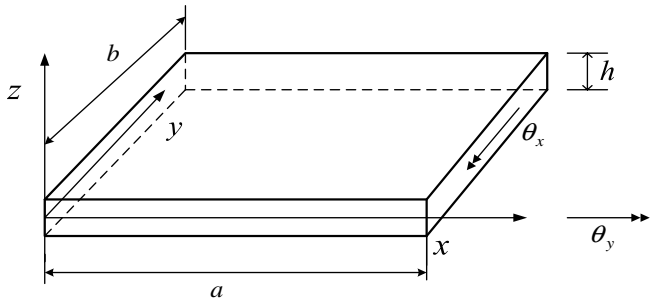

Fig. 2. Coordinate system of a plate.

represent the rotations of the transverse normal about the y and x axes, respectively (see Fig. 3).

The linear strains are given by

$$\begin{Bmatrix} \varepsilon_{xx} \\ \varepsilon_{yy} \\ \gamma_{xy} \end{Bmatrix} = \begin{Bmatrix} \frac{\partial u_0}{\partial x} \\ \frac{\partial v_0}{\partial y} \\ \frac{\partial u_0}{\partial y} + \frac{\partial v_0}{\partial x} \end{Bmatrix} - z \begin{Bmatrix} \frac{\partial \theta_x}{\partial x} \\ \frac{\partial \theta_y}{\partial y} \\ \frac{\partial \theta_x}{\partial y} + \frac{\partial \theta_y}{\partial x} \end{Bmatrix} = \{\boldsymbol{\varepsilon}_0\} - z\{\boldsymbol{\kappa}\}$$

$$\begin{Bmatrix} \gamma_{yz} \\ \gamma_{xz} \end{Bmatrix} = \begin{Bmatrix} \theta_y - \frac{\partial w_0}{\partial y} \\ \theta_x - \frac{\partial w_0}{\partial x} \end{Bmatrix} = \{\boldsymbol{\gamma}_0\} \tag{19}$$

The strain energy of the plate is expressed by

$$U_\varepsilon = \frac{1}{2}\int_\Omega \boldsymbol{\varepsilon}^{\mathrm{T}} \mathbf{S} \boldsymbol{\varepsilon}\, \mathrm{d}\Omega \tag{20}$$

where $\boldsymbol{\varepsilon}$ and $\mathbf{S}$ are given by

$$\boldsymbol{\varepsilon} = \begin{Bmatrix} \boldsymbol{\varepsilon}_0 \\ \boldsymbol{\kappa} \\ \boldsymbol{\gamma}_0 \end{Bmatrix} \tag{21}$$

$$\mathbf{S} = \begin{bmatrix} A_{11} & A_{12} & A_{16} & B_{11} & B_{12} & B_{16} & 0 & 0 \\ A_{12} & A_{22} & A_{26} & B_{12} & B_{22} & B_{26} & 0 & 0 \\ A_{16} & A_{26} & A_{66} & B_{16} & B_{26} & B_{66} & 0 & 0 \\ B_{11} & B_{12} & B_{16} & D_{11} & D_{12} & D_{16} & 0 & 0 \\ B_{12} & B_{22} & B_{26} & D_{12} & D_{22} & D_{26} & 0 & 0 \\ B_{16} & B_{26} & B_{66} & D_{16} & D_{26} & D_{66} & 0 & 0 \\ 0 & 0 & 0 & 0 & 0 & 0 & S_{44} & S_{45} \\ 0 & 0 & 0 & 0 & 0 & 0 & S_{45} & S_{55} \end{bmatrix} = \begin{bmatrix} \mathbf{A} & \mathbf{B} & \mathbf{0} \\ \mathbf{B} & \mathbf{D} & \mathbf{0} \\ \mathbf{0} & \mathbf{0} & \overline{\mathbf{S}} \end{bmatrix} = \begin{bmatrix} \overline{\mathbf{D}} & \mathbf{0} \\ \mathbf{0} & \overline{\mathbf{S}} \end{bmatrix} \tag{22}$$

In which the extensional (A_{ij}), coupling (B_{ij}), bending (D_{ij}) and transverse shear S_{ij} stiffnesses, are defined as

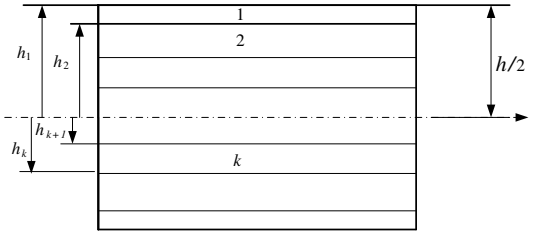

Fig. 3. Cross-sectional view of the laminated plate.

$$(A_{ij}, B_{ij}, D_{ij}) = \int_{-h/2}^{h/2} Q_{ij}(1, z, z^2)\mathrm{d}z, \quad S_{ij} = K\int_{-h/2}^{h/2} Q_{ij}\,\mathrm{d}z \tag{23}$$

where A_{ij}, B_{ij} and D_{ij} are defined for $i,j = 1,2,6$, whereas S_{ij} is defined for $i,j = 4,5$. K denotes the transverse shear correction coefficient.

For a plate composed of different layers of orthotropic materials, the stiffnesses can be defined as

$$A_{ij} = \sum_{k=1}^{N_l} \overline{Q}_{ij}^k (h_k - h_{k+1}), \quad B_{ij} = \frac{1}{2}\sum_{k=1}^{N_l} \overline{Q}_{ij}^k (h_k^2 - h_{k+1}^2)$$

$$D_{ij} = \frac{1}{3}\sum_{k=1}^{N_l} \overline{Q}_{ij}^k (h_k^3 - h_{k+1}^3), \quad S_{ij} = \frac{5}{6}\sum_{k=1}^{N_l} \overline{Q}_{ij}^k (h_k - h_{k-1}) \tag{24}$$

where h_k and h_{k+1} denote the distances from the plate reference mid-plane to the outer and inner surfaces of the kth layer, respectively, as shown in Fig. 3. N_l is the total number of layers in the laminated plate and $\overline{Q}_{ij}^k$ is the transformed reduced stiffness matrix for the kth layer and defined as

$$\overline{\mathbf{Q}} = \mathbf{T}^{-1}\mathbf{Q}\mathbf{T}^{-\mathbf{T}} \tag{25}$$

where $\mathbf{T}$ is the transformation matrix between the principle material coordinates and the plate's coordinates, and $\mathbf{Q}$ is the reduced stiffness matrix. Both $\mathbf{T}$ and $\mathbf{Q}$ can refer to the work by Reddy [37].

The external work done due to surface traction and body force is given by

$$W_{\mathrm{e}} = \int_\Omega \mathbf{u}^{\mathrm{T}}\bar{\mathbf{f}}\,\mathrm{d}\Omega + \int_\Gamma \mathbf{u}^{\mathrm{T}}\bar{\mathbf{t}}\,\mathrm{d}\Gamma \tag{26}$$

where $\bar{\mathbf{f}}$ and $\bar{\mathbf{t}}$ represent the external load and prescribed traction on the natural boundary, respectively.

For static analysis of plates, the total potential energy functional is expressed as

$$\Pi_{\mathrm{s}} = U_\varepsilon - W_{\mathrm{e}} \tag{27}$$

For free vibration analysis of plates, the kinetic energy of the plates is given by

$$\Theta = \frac{1}{2}\int_\Omega \rho h(\dot{u}^2 + \dot{v}^2 + \dot{w}^2)\mathrm{d}\Omega \tag{28}$$

the total energy functional is thus given by

$$\Pi_v = U_\varepsilon - \Theta \tag{29}$$

4.2. Nodal distribution and integration

4.2.1. Static analysis

The approximations of displacements and rotations of the mid-plane of the plate are expressed using RPIM shape functions as

$$\mathbf{u}_0^h = \begin{pmatrix} u_0^h \\ v_0^h \\ w_0^h \\ \theta_x^h \\ \theta_y^h \end{pmatrix} = \sum_{I=1}^{\mathrm{NP}} \phi_{\mathrm{I}}(\mathbf{x}) \begin{pmatrix} u_{\mathrm{I}} \\ v_{\mathrm{I}} \\ w_{\mathrm{I}} \\ \theta_{xI} \\ \theta_{yI} \end{pmatrix} = \sum_{I=1}^{\mathrm{NP}} \phi_{\mathrm{I}}(\mathbf{x})\mathbf{d}_{\mathrm{I}} \tag{30}$$

Substituting Eq. (30) into Eq. (27) and taking variation to the energy functional yield the equilibrium equation

$$\mathbf{K}\mathbf{d} = \mathbf{f} \tag{31}$$

where

$$\mathbf{K} = \mathbf{K}^b + \mathbf{K}^s \tag{32}$$

$$\mathbf{d}^{\mathrm{T}} = [\mathbf{d}_1^{\mathrm{T}} \quad \mathbf{d}_2^{\mathrm{T}}, \ldots, \mathbf{d}_n^{\mathrm{T}}] \tag{33}$$

$$\mathbf{K}_{\mathrm{IJ}}^b = \int_\Omega \mathbf{B}_{\mathrm{I}}^{b^{\mathrm{T}}} \overline{\mathbf{D}} \mathbf{B}_J^b \, \mathrm{d}\Omega \tag{34}$$

$$\mathbf{K}_{\mathrm{IJ}}^s = \int_\Omega \mathbf{B}_{\mathrm{I}}^{s^{\mathrm{T}}} \overline{\mathbf{S}} \mathbf{B}_J^s \, \mathrm{d}\Omega \tag{35}$$

$$\mathbf{f}_{\mathrm{I}} = \int_\Omega \phi_{\mathrm{I}} \bar{\mathbf{f}} \, \mathrm{d}\Omega + \int_\Gamma \phi_{\mathrm{I}} \bar{\mathbf{t}} \, \mathrm{d}\Gamma \tag{36}$$

By applying the strain smoothing technique introduced in Section 3, the integrals of Eqs. (34)–(36) are approximated by performing nodal integration as follows:

$$\mathbf{K}_{\mathrm{IJ}}^b = \sum_{L=1}^{\mathrm{NP}} \widetilde{\mathbf{B}}_I^{b^{\mathrm{T}}}(\mathbf{x}_L) \overline{\mathbf{D}} \widetilde{B}_J^b(\mathbf{x}_L) A_L \tag{37}$$

$$\mathbf{K}_{\mathrm{IJ}}^s = \sum_{L=1}^{\mathrm{NP}} \mathbf{B}_{\mathrm{I}}^{s^{\mathrm{T}}}(\mathbf{x}_L) \overline{\mathbf{S}} \mathbf{B}_J^s(\mathbf{x}_L) A_L \tag{38}$$

$$\mathbf{f}_{\mathrm{I}} = \sum_{L=1}^{\mathrm{NP}} \phi_{\mathrm{I}}(\mathbf{x}_L)\mathbf{f}(\mathbf{x}_L) A_L + \sum_{L=1}^{NPb} \phi_{\mathrm{I}}(\mathbf{x}_L)\bar{\mathbf{t}}(\mathbf{x}_L) s_L \tag{39}$$

where $\mathbf{x}_L$ and A_L are nodal point coordinate and the nodal representative area, respectively, NP^b is the number of nodes on the natural boundary, and s_L is the weight associated with the boundary point obtained from Voronoi diagram or Delaunay triangulation. $\widetilde{\mathbf{B}}_{\mathrm{I}}^b(\mathbf{x}_L)$ and $\mathbf{B}_{\mathrm{I}}^s(\mathbf{x}_L)$ are given by

$$\widetilde{\mathbf{B}}_{\mathrm{I}}^b(\mathbf{x}_L) = \begin{bmatrix} \tilde{b}_{\mathrm{I}x}(\mathbf{x}_L) & 0 & 0 & 0 & 0 \\ 0 & \tilde{b}_{\mathrm{I}y}(\mathbf{x}_L) & 0 & 0 & 0 \\ \tilde{b}_{\mathrm{I}y}(\mathbf{x}_L) & \tilde{b}_{\mathrm{I}x}(\mathbf{x}_L) & 0 & 0 & 0 \\ 0 & 0 & 0 & \tilde{b}_{\mathrm{I}x}(\mathbf{x}_L) & 0 \\ 0 & 0 & 0 & 0 & \tilde{b}_{\mathrm{I}y}(\mathbf{x}_L) \\ 0 & 0 & 0 & \tilde{b}_{\mathrm{I}y}(\mathbf{x}_L) & \tilde{b}_{\mathrm{I}x}(\mathbf{x}_L) \end{bmatrix} \tag{40}$$

$$\tilde{b}_{\mathrm{I}x}(\mathbf{x}_L) = \frac{1}{A_L} \int_{\Gamma_L} \phi_{\mathrm{I}}(\mathbf{x}) n_x(\mathbf{x}) \, \mathrm{d}\Gamma \tag{41}$$

$$\tilde{b}_{\mathrm{I}y}(\mathbf{x}_L) = \frac{1}{A_L} \int_{\Gamma_L} \phi_{\mathrm{I}}(\mathbf{x}) n_y(\mathbf{x}) \, \mathrm{d}\Gamma \tag{42}$$

$$\mathbf{B}_{\mathrm{I}}^s(\mathbf{x}_L) = \begin{bmatrix} 0 & 0 & \frac{\partial \phi_{\mathrm{I}}(\mathbf{x}_L)}{\partial x} & -\phi_{\mathrm{I}}(\mathbf{x}_L) & 0 \\ 0 & 0 & \frac{\partial \phi_{\mathrm{I}}(\mathbf{x}_L)}{\partial y} & 0 & -\phi_{\mathrm{I}}(\mathbf{x}_L) \end{bmatrix} \tag{43a}$$

$$\text{or } \mathbf{B}_{\mathrm{I}}^s(\mathbf{x}_L) = \begin{bmatrix} 0 & 0 & \tilde{b}_{\mathrm{I}x}(\mathbf{x}_L) & -\phi_{\mathrm{I}}(\mathbf{x}_L) & 0 \\ 0 & 0 & \tilde{b}_{\mathrm{I}y}(\mathbf{x}_L) & 0 & -\phi_{\mathrm{I}}(\mathbf{x}_L) \end{bmatrix} \tag{43b}$$

If the strain smoothing technique is applied only to matrix $\mathbf{B}_{\mathrm{I}}^b$, which takes the form in Eq. (40), and matrix $\mathbf{B}_{\mathrm{I}}^s$ takes the form in Eq. (43a), the smoothing scheme is defined as curvature smoothing (CS). If $\mathbf{B}_{\mathrm{I}}^b$ and $\mathbf{B}_{\mathrm{I}}^s$ are expressed as in Eqs. (40) and (43b), the smoothing scheme is called curvature and shear strain smoothing (CSS). Therefore, there are two ways in evaluating $\mathbf{B}_{\mathrm{I}}^s(\mathbf{x}_L)$. Eqs. (41) and (42) can be evaluated using Trapezoidal rule or Gauss quadrature on the boundaries of representative nodal domain.

4.2.2. Free vibration analysis

For vibration analysis, the approximations of displacements and rotations of the mid-plane of the plate are expressed by RPIM shape functions as

$$\mathbf{u}_0^h = \sum_{I=1}^{\mathrm{NP}} \phi_{\mathrm{I}}(\mathbf{x})\mathbf{d}_{\mathrm{I}} \mathrm{e}^{\mathrm{i}\omega t} \tag{44}$$

Substituting Eq. (44) into Eq. (29) and taking variation to the energy functional yield the eigen equation

$$(\mathbf{K} - \omega^2 \mathbf{M})\mathbf{d} = 0 \tag{45}$$

where $\mathbf{K}$ and $\mathbf{d}$ have the same expressions as those given in Eqs. (32) and (33), and mass matrix $\mathbf{M}$ is given by

$$\mathbf{M}_{\mathrm{I}J} = \int_\Omega \mathbf{G}_{\mathrm{I}}^{\mathrm{T}} \mathbf{m} \mathbf{G}_J \, \mathrm{d}\Omega \tag{46}$$

The matrix $\mathbf{M}$ is evaluated using nodal integration as

$$\mathbf{M}_{\mathrm{I}J} = \sum_{L=1}^{\mathrm{NP}} \mathbf{G}_{\mathrm{I}}^{\mathrm{T}}(\mathbf{x}_L) \mathbf{m} \mathbf{G}_J(\mathbf{x}_L) A_L \tag{47}$$

where

$$\mathbf{G}_{\mathrm{I}}(\mathbf{x}_L) = \begin{bmatrix} \phi_{\mathrm{I}}(\mathbf{x}_L) & 0 & 0 & 0 & 0 \\ 0 & \phi_{\mathrm{I}}(\mathbf{x}_L) & 0 & 0 & 0 \\ 0 & 0 & \phi_{\mathrm{I}}(\mathbf{x}_L) & 0 & 0 \\ 0 & 0 & 0 & \phi_{\mathrm{I}}(\mathbf{x}_L) & 0 \\ \mathbf{0} & 0 & 0 & 0 & \phi_{\mathrm{I}}(\mathbf{x}_L) \end{bmatrix} \tag{48}$$

$$\mathbf{m} = \begin{bmatrix} \rho h & 0 & 0 & 0 & 0 \\ 0 & \rho h & 0 & 0 & 0 \\ 0 & 0 & \rho h & 0 & 0 \\ 0 & 0 & 0 & \frac{1}{12}\rho h^3 & 0 \\ 0 & 0 & 0 & 0 & \frac{1}{12}\rho h^3 \end{bmatrix} \tag{49}$$

The frequencies and corresponding mode shapes can be obtained by solving the eigenvalue equation.

5. Numerical examples

In this section, examples for plate bending and vibration analyses are presented. The displacement shape functions are constructed using radial point interpolation method. The shape parameters q and R_c are taken as 1.03 and 1.42, respectively. The scaling factor of influence domain of 3.0 is selected. The nodal integration domain is obtained by connecting the centroid and mid-point of edges of each

triangle, which created by Delaunay triangulation. Trapezoidal rule with two-point on each segment for integration is adopted. Curvature strain smoothing (CS) model is adopted in all examples, except for shear-locking test case. The material properties, unless specified otherwise, are taken as Young's modulus $E = 1.0 \times 10^9 \mathrm{N/m}^2$, Poisson ratio $v = 0.3$.

5.1. Plate bending

5.1.1. Square plates

A square plate subjected to transverse uniform load is first analyzed, the geometry properties of the plate are given as: length $a = 10$ and thickness $h = 1$. The nodal representative domain for nodal integration is obtained from Delaunay triangulation. A nodal representative domain with regular node distribution is given in Fig. 4. Convergence studies are performed based on the influence of the number of nodes for plates with simply supported and clamped boundary conditions. The present solutions are normalized with those given by Zienkiewicz and Taylor [38], where the central deflections of the plate are 0.004280 and 0.001580 for simply-supported and clamped plates, respectively. A comparison of convergence characteristics for plates with different edge constraints is shown in Fig. 5. A monotonically convergent trend is observed for the simply-supported plate, while an oscillation is noticed in the curve for clamped plate when fewer nodes are used. Similar trend, however, is clearly seen as the number of nodes increases for both cases. It is concluded that the present method shows good convergence performance for square plate analysis.

In order to investigate the stability of present approach, the effects of irregular node distributions are studied. The irregularly distributed nodes are generated by manipulating the regular nodes according to the following approach

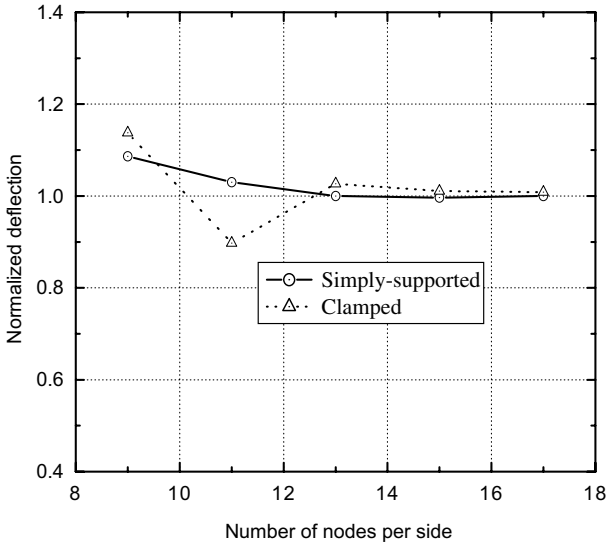

Fig. 5. Convergence comparison for plates with different boundary conditions.

$$x_{\mathrm{ir}} = x + \Delta x \cdot r_c \cdot \alpha_{\mathrm{ir}}$$
$$y_{\mathrm{ir}} = y + \Delta y \cdot r_c \cdot \alpha_{\mathrm{ir}} \tag{50}$$

where x and y are the coordinates of regular nodes, Δx and Δy are initial nodal spacings, r_c is a random number between -1 and 1, α_{ir} represents the irregularity factor ranging from 0.1 to 0.4. An example of representative nodal domain for irregular node distribution is shown in Fig. 6. The number of nodes used in this example is 121. Fig. 7 elucidates the effects of irregularity factor α_{ir} on the central deflections of the plate. It is observed that the maximum error is less than 2% when the irregularity factor α_{ir} is taken as high as 0.4. It is concluded that the irregularity of nodal distribution produced according to Eq. (50) does not influence the solutions significantly. It is also found that the error due to the irregularity of nodal distribution can be

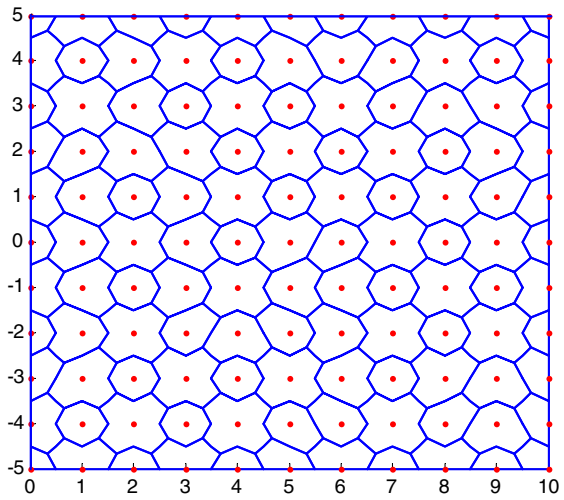

Fig. 4. A uniform nodal distribution in a square plate.

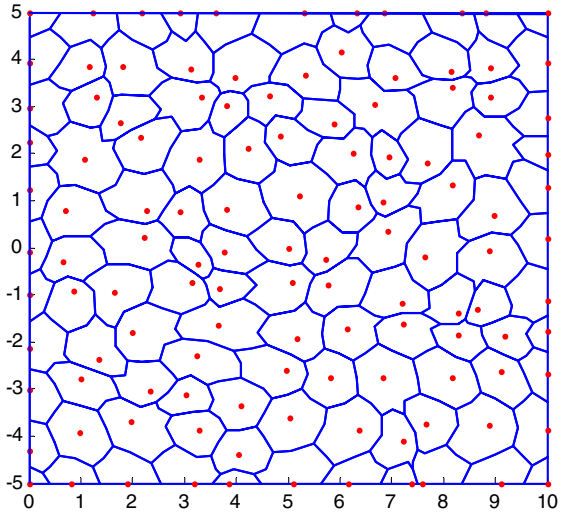

Fig. 6. An irregular nodal distribution in a square plate. $\alpha_{ir} = 0.4$.

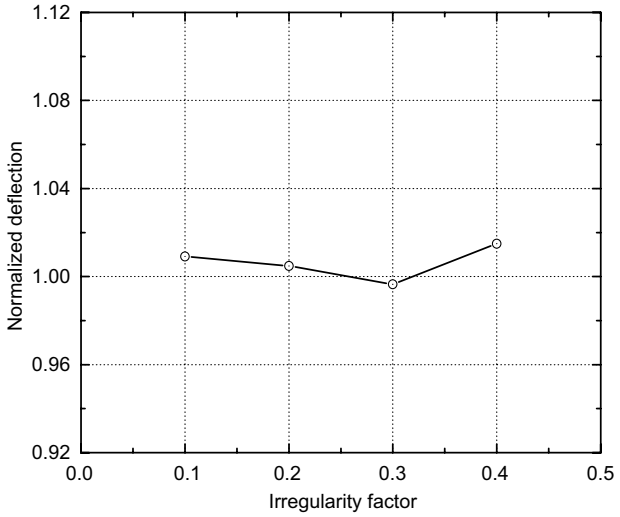

Fig. 7. Effects of irregular node distribution.

reduced by adding more nodes, which is clearly observed in Fig. 8.

A further study, the influence of highly irregular node distribution on solutions, is carried out for square plates under uniform or point loads. The extremely irregular nodes are generated randomly. Two nodal distribution schemes are tested. Fig. 9 shows a plate with regularly distributed nodes on boundaries and highly irregular nodes scattered on the inside of the plate. An extremely irregular node distribution on entire plate is given in Fig. 10. An error up to 7.8% is found for nodal distribution scheme shown in Fig. 10. The error, however, can be reduced to less than 3% when the scheme with regularly distributed boundary nodes, shown in Fig. 9, is applied. It demonstrates that the distribution of boundary nodes has significant effects on solutions when the nodal distribution is highly irregular.

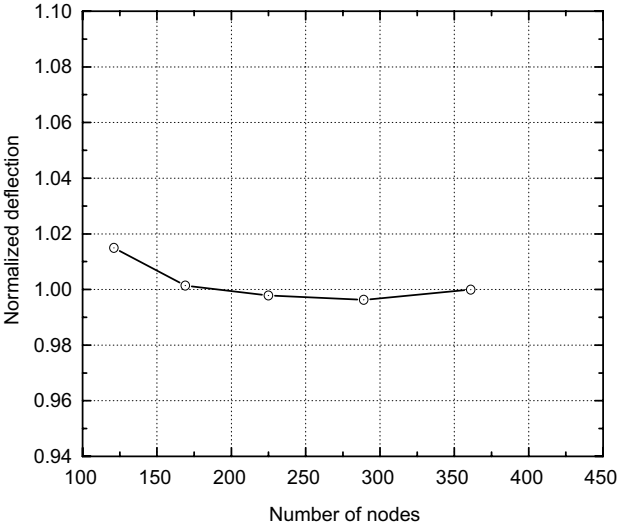

Fig. 8. Effects of the irregularity of the nodal distribution.

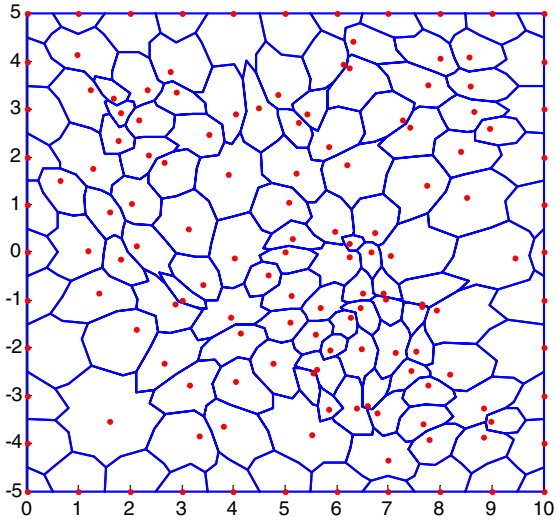

Fig. 9. Extremely irregular node distribution in the inside of a square plate.

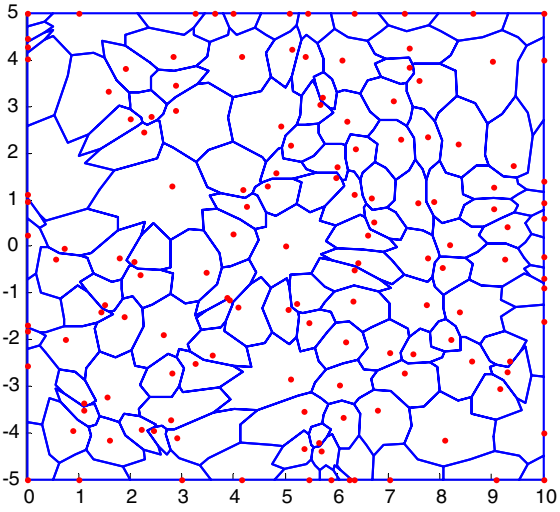

Fig. 10. Highly irregular node distribution in a square plate.

5.1.2. Circular plates

Clamped circular plates subjected to a centre point load and uniform load are analyzed in this part. Due to the symmetry, the problem can either be modeled on entire domain or on a quarter of plates. A nodal distribution of a full plate with 401 nodes is shown in Fig. 11. The load is directly applied on the node located at the center of the plate. The radius of the plate is $R = 10$ and the thickness is $h = 0.1$. The analytical solutions for deflections are given by [39]

$$w(r) = \frac{q}{64D}(R^2 - r^2)^2 \quad \text{(for uniform load)} \tag{51}$$

$$w(r) = \frac{qR^2}{16\pi D}\left[1 - \left(\frac{r}{R}\right)^2 + 2\left(\frac{r}{R}\right)^2 \ln\frac{r}{R}\right] \quad \text{(for point load)} \tag{52}$$

where r is the distance gauged from the plate centre, and $D = Eh^3/12(1 - \nu^2)$ is the bending stiffness. Table 1 shows

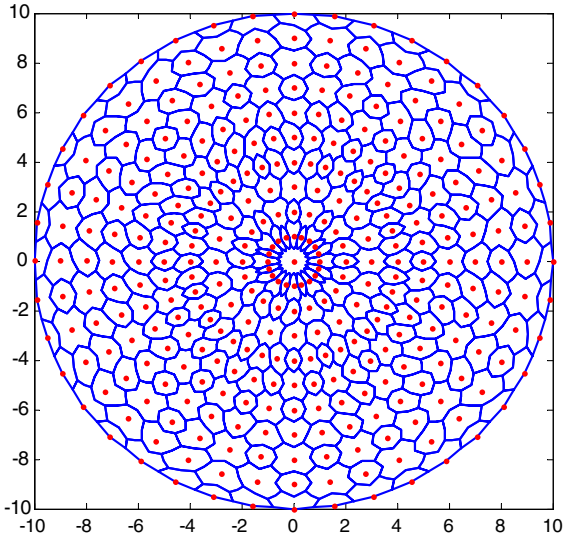

Fig. 11. Nodal distribution in a circular plate.

Table 1
Non-dimensional central deflections of a clamped circular plate ($R = 10$, $h = 0.1$)

Load	Central deflection	
	Present	Analytical [39]
Uniform load	0.0159948	0.015625
Point load	0.019932	0.019932

the comparison of present normalized central deflections with analytical solutions. The normalized deflections $\bar{w} = wD/qR^2$ for point load case and $\bar{w} = wD/q$ for uniform loading are tabulated in Table 1. Good agreements are observed from comparisons.

5.1.3. Shear-locking test

Shear-locking in plate is caused by the parasitic shear, which is generated due to the inability of the formulation based on the first order deformation theory in reproducing pure bending mode. In this section, we utilize RPIM shape functions in the shear deformable plate formulation to investigate the shear-locking. Two strain smoothing schemes, curvature smoothing (CS) only and both curvature and shear strain smoothing (CSS), are performed for square plates with side length $a = 10$ under uniform load q. The deflection is normalized as $\hat{w} = wD/qa^4$. Fig. 12 shows the locking test results for a simply-supported square plate. Both smoothing schemes give satisfactory results for relatively thicker plate. As the plate becomes thinner, however, a significant locking is observed when CCS scheme is applied, whereas the CS scheme produces a locking-free solution and agrees with the exact thin plate solution. The numerical results demonstrate that the shear strain smoothing produces additional stiffening effects on structural rigidity and triggers shear-locking for thin plates. Similar results are also observed from Fig. 13 for a clamped square plate. In this case, the deflection is normalized as

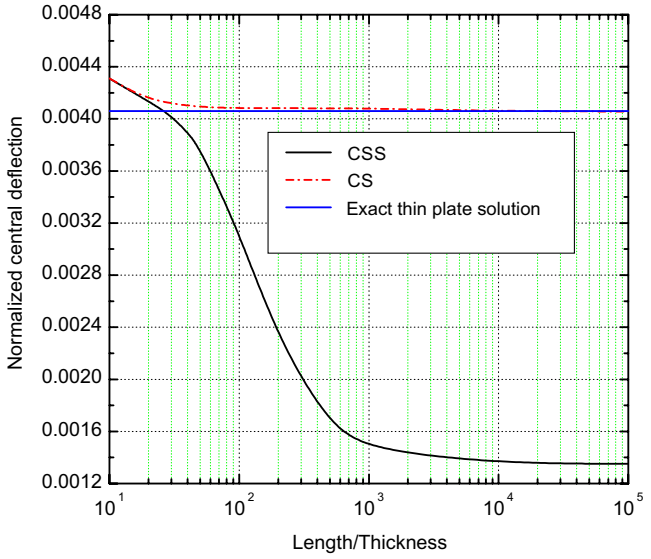

Fig. 12. Shear-locking test for a simply-supported square plate. (CS: -·-·—; CSS: —-).

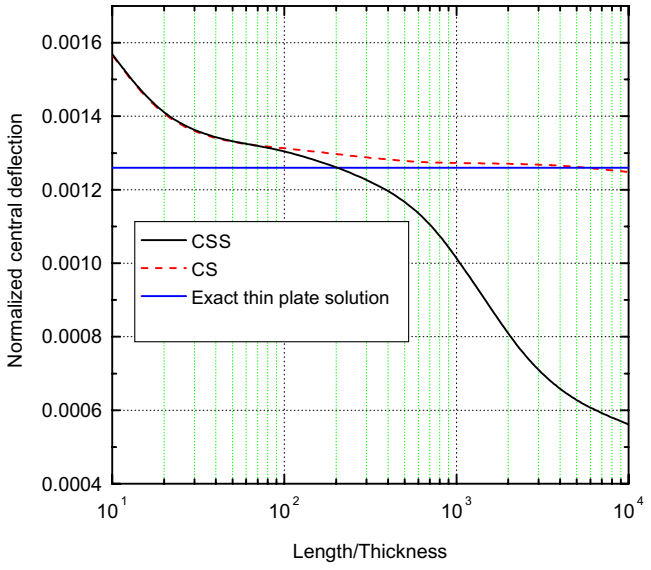

Fig. 13. Shear-locking test for a clamped square plate. (CS: -·-·—; CSS: —-).

$\hat{w} = wD/qa^2$. Therefore, CS model should be used for thin plate analysis in order to eradicate shear-locking.

5.1.4. Laminated composite plates

In this section, we consider laminates that are simply supported on two opposite edges and subjected to three different boundary conditions on the other two edges. For each laminate, a quarter of the plate is modeled, and total 361 nodes are used to obtain convergent solution. The material properties of the laminates are: $E_1/E_2 = 25$, $G_{12} = G_{13} = 0.5E_2$, $G_{23} = 0.2E_2$, $\nu_{12} = 0.25$. The laminates are subjected to uniform loading q_0 or sinusoidal loading $q(x,y) = q_0 \cos(\pi x/a) \sin(\pi y/b)$. The normalized maximum

deflection is defined as $\bar{w} = 100wE_2h^3/a^4q_0$, and the stresses are normalized as $\bar{\sigma}_{xx} = 10\sigma_{xx}h^2/a^2q$, $\bar{\sigma}_{yy} = 10\sigma_{yy}h^2/a^2q$ and $\bar{\sigma}_{yz} = 10\sigma_{yz}h/aq$. For two-layer cross-ply (0°/90°) and three-layer cross-ply (0°/90°/90°) square plates under sinusoidal loading, Table 2 shows the comparison of present results with solutions given by Khdeir and Reddy [40] and Vel and Batra [21]. Most differences are less than 1% and the maximum does not exceed 4%. Table 3 provides the solutions of normalized stresses obtained from RPIM and those given by Vel and Batra[21] and Khdeir and Reddy [40]. It is observed that the RPIM solutions are close to analytical solutions [21] and agree well with results given by Keheir and Reddy [40] for normal stresses. The transverse stresses, however, are different with the analytical values, which are more accurate because the transverse stresses are calculated from equilibrium instead of constitutive relations, which are employed in present study. Table 4 contains the comparison of the present solutions with those given by Reddy and Miravete [41] for antisymmetric angle-ply (45°/−45°/45°/−45°) square laminates under uniform loading. The other material properties are same as those in Table 4 except the Young's modules. Very good agreement is observed.

Table 3
Nondimensionalized stresses for laminated square plates under sinusoidal loading

a/h		Variable	0°/90°		
			SSSS	SSCC	SSFF
5	Present	$\bar{\sigma}_{xx}(0)$	7.161	4.012	2.501
		$\bar{\sigma}_{yy}(h)$	7.161	5.183	11.985
		$\bar{\sigma}_{yz}(h/2)$	2.726	1.961	3.869
	Vel and Batra [21]	$\bar{\sigma}_{xx}(0)$	7.671	4.630	2.660
		$\bar{\sigma}_{yy}(h)$	7.894	5.723	12.877
		$\bar{\sigma}_{yz}(h/2)$	1.211	0.875	1.541
	Khdeir and Reddy [40]	$\bar{\sigma}_{xx}(0)$	7.157	3.911	2.469
		$\bar{\sigma}_{yy}(h)$	7.157	5.153	11.907
		$\bar{\sigma}_{yz}(h/2)$	2.729	1.958	3.901
10	Present	$\bar{\sigma}_{xx}(0)$	7.160	4.462	2.440
		$\bar{\sigma}_{yy}(h)$	7.160	3.801	11.886
		$\bar{\sigma}_{yz}(h/2)$	2.724	1.522	3.878
	Vel and Batra [21]	$\bar{\sigma}_{xx}(0)$	7.304	4.653	2.503
		$\bar{\sigma}_{yy}(h)$	7.309	3.888	12.100
		$\bar{\sigma}_{yz}(h/2)$	1.219	0.713	1.490
	Khdeir and Reddy [40]	$\bar{\sigma}_{xx}(0)$	7.157	4.450	2.442
		$\bar{\sigma}_{yy}(h)$	7.157	3.799	11.884
		$\bar{\sigma}_{yz}(h/2)$	2.729	1.523	3.882

Table 4
Nondimensionalized deflections for an angle-ply square plate (45°/−45°/45°/−45°) under uniform loading ($a/h = 10$)

E_1/E_2		SSSS	SSCC	SSFF
10	Present	1.1604	0.7728	6.0155
	Reddy and Miravete [41]	1.1598	0.7708	6.0487
20	Present	0.7056	0.5198	4.2508
	Reddy and Miravete [41]	0.7013	0.5180	4.2843
30	Present	0.5360	0.4192	3.2606
	Reddy and Miravete [41]	0.5312	0.4170	3.2417

5.2. Free vibration of plates

In the following examples, free vibrations of various plates are analyzed, and rotary inertia (RI) is taken into account in present study. The nodal integration domain is generated using Delaunay triangulation. Solutions are obtained using two-point Trapezoidal integration rule. A scaling factor of 3.0 is used throughout this study.

5.2.1. Isotropic plate

A simply-supported isotropic square plate having uniformly distributed nodes, shown in Fig. 4, is investigated. The geometry and material properties of the plate are: density $\rho = 8000\ \mathrm{kg/m^2}$, Young's modulus $E = 2.0 \times 10^{11}\ \mathrm{N/m^2}$, Poisson's ratio $v = 0.3$, and dimension length to thickness ratio $a/h = 10$. The nondimensional frequency parameter is defined as $\bar{\omega} = \omega a^2\sqrt{\rho/Eh^2}$. The node number ranges from 169 to 361. Table 5 shows the comparison of present solutions with exact solutions of the 3D elastic theory [19] and those given by Reddy [37], frequency parameters for four modes are provided in the table. The solutions of stresses for mode (3, 3) are also compared with exact values given by Srinivas et al. [19] in Table 6. From these two tables, it is found that the present method shows good convergence and gives stable and accurate solutions.

5.2.2. Laminated composite plate

Two simply supported symmetric cross-ply (0°/90°/0°) square plates are considered, the length to thickness ratios are $a/h = 10$ and $a/h = 100$, respectively. The material

Table 2
Nondimensionalized displacements for laminated square plates under sinusoidal loading

a/h		0°/90°			0°/90°/0°		
		SSSS	SSCC	SSFF	SSSS	SSCC	SSFF
5	Present	1.762	1.259	2.789	1.562	1.201	5.249
	Vel and Batra [21]	1.712	1.217	2.753	1.525	1.18	5.307
	Khdeir and Reddy [40]	1.758	1.257	2.777	–	–	–
10	Present	1.245	0.665	2.031	0.7531	0.448	4.335
	Vel and Batra [21]	1.227	0.648	2.026	0.753	0.446	4.453
	Khdeir and Reddy [40]	1.237	0.656	2.028	–	–	–

Table 5
Nondimensionalized natural frequencies of a simply supported isotropic square plate with RI ($\bar{\omega} = \omega a^2\sqrt{\rho/Eh^2}$, $v = 0.3$, $a/h = 10$)

Mode	Number of nodes	$\bar{\omega}$		
		Present	Srinivas et al. [19]	Reddy [37]
1	169	5.687	5.767	5.769
	225	5.681		
	289	5.722		
	361	5.728		
	441	5.728		
2	169	13.375	13.753	13.764
	225	13.469		
	289	13.526		
	361	13.543		
	441	13.543		
3	169	20.154	21.097	21.121
	225	20.118		
	289	20.569		
	361	20.571		
	441	20.570		
4	169	25.17	25.700	25.734
	225	25.147		
	289	25.018		
	361	25.349		
	441	25.350		

Table 6
Variations of stresses across the isotropic square plate ($v = 0.3$, $a/h = 10$)

z/h	$\sigma_x/\sigma_x(h/2)$		$\tau_{xy}/\tau_{xy}(h/2)$	
	Present	Srinivas [19]	Present	Srinivas [19]
0.1	0.7602	0.7676	0.7512	0.7561
0.2	0.5521	0.5571	0.5391	0.5420
0.3	0.3605	0.3627	0.3464	0.3496
0.4	0.1756	0.1787	0.1695	0.1713

parameters are $\rho = 1643\ \text{kg/m}^3$, $E_{22} = 7.6 \times 10^9\ \text{N/m}^2$, $E_{11} = 25E_{22}$, $G_{12} = G_{13} = 0.5E_{22}$, $G_{23} = 0.2E_{22}$, and $v_{12} = 0.25$. A nodal distribution model having 15×15 nodes is used in the analysis. Both present results and Reddy's solutions [37] are provided in Table 7 for comparison purpose. In general, good agreement is observed for all modes.

5.2.3. Square plate with a square hole at the centre

Free vibration of a simply-supported square plate with a square cutout at the centre, shown in Fig. 14, is analyzed. The geometry and material parameters are length $a = 10$, size ratio $a_0/a = 0.5$, thickness ration $h/a = 0.01$, density $\rho = 8000\ \text{kg/m}^2$, Young's modulus $E = 2.0 \times 10^{11}\text{N/m}^2$, Poisson's ratio $v = 0.3$. A nodal distribution is shown in Fig. 15. The present results are obtained using total 216 nodes. The solution normalization $\tilde{\omega} = [\rho h\omega^2 a^4/D(1-v^2)]^{1/4}$ is used. The present results are compared with solutions given by Huang and Sakiyama [42], Ali and Atwal [43] in Table 8. It is observed that good agreements are attained with Huang and Sakiyama [42] for eleven modes, and with Ali and Atwal [43] for the first five modes.

Table 7
Nondimensionalized natural frequencies of simply supported symmetric cross-ply (0°/90°/0°) square plates with RI ($\bar{\omega} = \omega a^2\sqrt{\rho/E_{22}h^2}$, $E_{11} = 25E_{22}$, $G_{12} = G_{13} = 0.5E_{22}$, $G_{23} = 0.2E_{22}$, $v_{12} = 0.25$)

a/h	Mode	Present	Reddy [37]
10	1	11.455	12.163
	2	18.333	18.729
	3	31.141	30.931
100	1	15.127	15.183
	2	22.658	22.817
	3	39.644	40.153
	4	55.452	56.210
	5	59.289	60.211

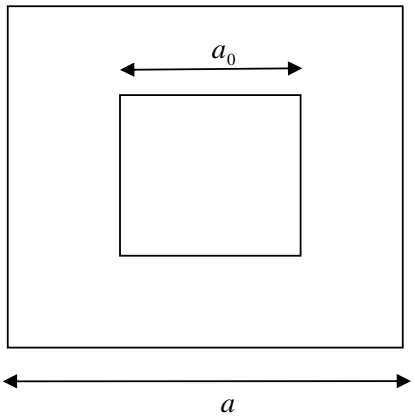

Fig. 14. A square plate with a square hole.

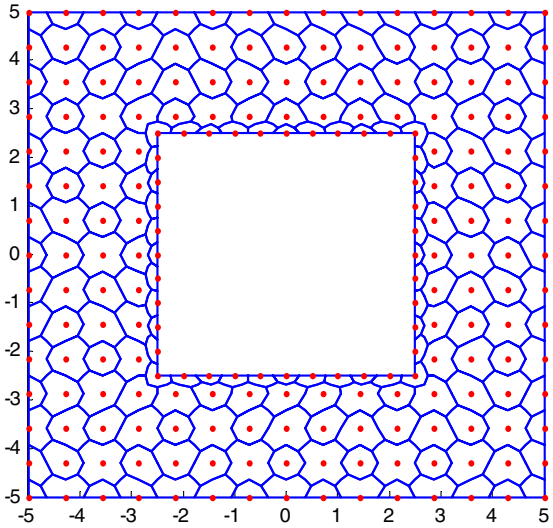

Fig. 15. A nodal distribution in a square plate with a square hole.

5.2.4. Square plate with a circular cutout

Consider a square plate with a circular cutout at the centre shown in Fig. 16, the length of the plate is $a = 10$, the ratio of the radius to length is $R_0/a = 0.1$, and the thickness

Table 8
Nondimensionalized natural frequencies of simply supported square plates with a square hole at the centre ($\tilde{\omega} = [\rho h \omega^2 a^4/D(1-v^2)]^{1/4}$, $h/a = 0.01$)

Mode	Present	Huang and Sakiyama [42]	Ali and Atwal [43]
1	4.9217	4.839	4.936
2	6.4810	6.435	6.502
3	6.4821	6.440	6.502
4	8.5509	8.492	8.525
5	8.8656	8.875	8.813
6	10.720	10.805	–
7	10.767	10.831	–
8	12.045	12.291	
9	13.370	13.534	
10	14.180	14.108	
11	14.208	14.234	

ratio is $h/a = 0.01$. The material properties in Section 5.2.3 are used. A nodal distribution model with 225 nodes is shown in Fig. 17. Table 9 shows the comparison of present results with solutions by Huang and Sakiyama [42] for a clamped plate. The fundamental frequencies for a simply-supported plate and a clamped plate are computed and compared with solutions by Belvins [44] in Table 10. It is observed that the fundamental frequency agrees well with results by both Belvins [44]. The present solutions for the other frequencies are little higher, but the maximum difference does not exceed 4%.

5.2.5. Square plate with a complicated cutout

A square plate with a complicated cutout is analyzed in this section. The thickness of the plate is $h = 0.05$, the other dimensions are shown in Fig. 18. The material properties in Section 5.2.1 are used. Fig. 19 shows a nodal distribution of the plate. The natural frequencies for simply-supported and clamped plates are tabulated in Table 11. For comparison purpose, solutions obtained from ANSYS are also listed. It is observed that good agreements are attained, especially for fundamental frequency. For modes 7 and 8 of the simply-supported plate, and modes 4, 5 and 6 for clamped plate, the present solutions are little lower than

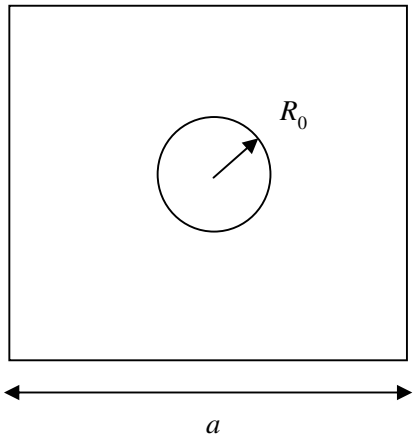

Fig. 16. A square plate with a circular hole.

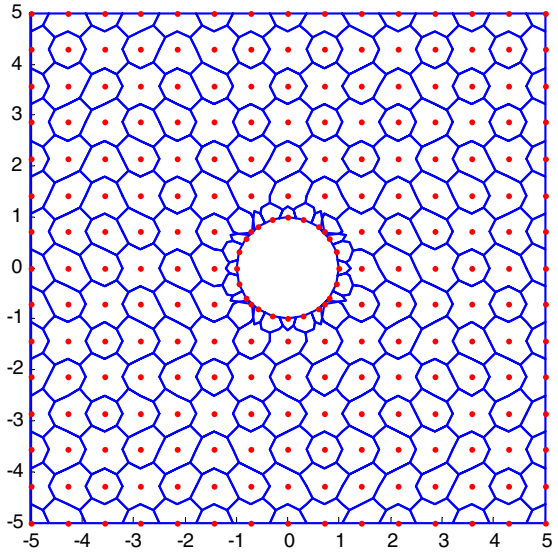

Fig. 17. A nodal distribution in a square plate with a circular cutout.

Table 9
Nondimensionalized natural frequencies of clamped square plates with a circular hole at the centre ($\tilde{\omega} = [\rho h \omega^2 a^4/D(1-v^2)]^{1/4}$, $h/a = 0.01$, $r/a = 0.1$)

Mode	Present	Huang and Sakiyama [42]
1	6.149	6.240
2	8.577	8.457
3	8.634	8.462
4	10.422	10.233
5	11.414	11.719
6	11.838	12.299
7	12.829	13.037
8	12.842	13.041

Table 10
Nondimensionalized fundamental natural frequencies of square plates with a circular hole at the centre ($\hat{\omega} = \omega a^2\sqrt{\rho/D}$, $h/a = 0.01$, $R_0/a = 0.1$)

Boundary condition	Present	Blevins [44]
SSSS	19.258	19.300
CCCC	36.060	35.700

results computed using ANSYS, and the maximum difference is less than 5%.

5.2.6. Laminated composite plate

Laminated composite plates with different angle-ply schemes are studied in this section. The dimensionless frequencies, $\bar{\omega} = \omega a^2\sqrt{\rho/E_2 h^2}$, of angle-ply laminates ($\beta/-\beta/\beta/\ldots$), under three different boundary conditions and with different values of β are presented in Table 12. The material properties are $E_1/E_2 = 40$, $G_{12} = G_{13} = 0.6E_2$, $G_{23} = 0.5E_2$, $v_{12} = 0.25$. Total 289 nodes are used to attain the convergent solution. The solutions by Reddy and

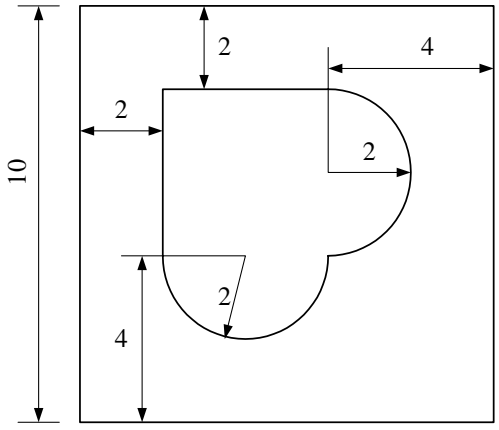

Fig. 18. A square plate with a complicated cutout.

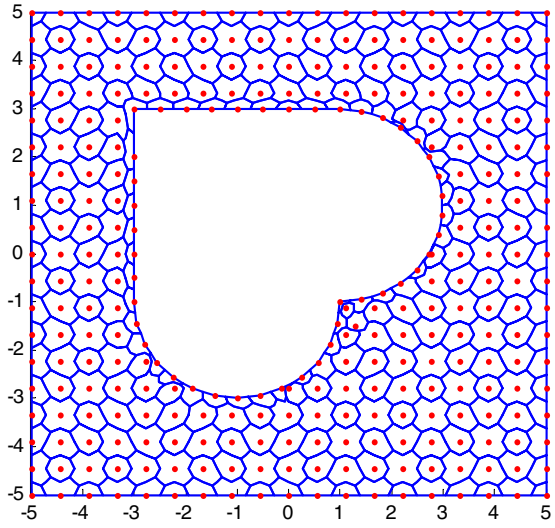

Fig. 19. A nodal distribution in a square plate with a complicated cutout.

Table 11
Natural frequencies of square plates with a complicated hole ($h = 0.05$)

Mode	SSSS		CCCC	
	Present (Hz)	ANSYS (Hz)	Present (Hz)	ANSYS (Hz)
1	2.9060	2.9058	6.5903	6.6624
2	4.8352	4.9179	11.249	11.593
3	5.4402	5.4895	11.261	11.652
4	8.6481	8.8213	13.990	14.428
5	9.6034	9.6779	14.569	15.003
6	13.492	13.651	17.881	18.353
7	13.936	14.270	19.190	19.831
8	15.862	16.200	21.147	21.769
9	19.251	19.759	24.295	25.182
10	20.396	20.816	25.175	26.105
11	24.993	25.815	31.446	31.779
12	25.649	26.562	32.459	32.539

Miravete [41] are also listed in Table 10 for comparison purpose. It is observed that the present solutions agree well with those given by Reddy and Miravete [41].

Table 12
Dimensionless fundamental frequency $\bar{\omega} = \omega a^2\sqrt{\rho/E_2h^2}$ for 10-layer angle-ply square plates ($\beta/-\beta/\beta/\cdots/-\beta$, $a/h = 10$)

β		SSSS	SSCC	SSFF
30°	Present	18.33	19.79	3.85
	Reddy and Miravete [41]	18.51	19.81	3.82
45°	Present	19.29	21.06	6.58
	Reddy and Miravete [41]	19.38	21.25	6.57
60°	Present	18.33	21.02	10.12
	Reddy and Miravete [41]	18.51	21.21	10.11

6. Conclusions

A formulation has been presented for static and free vibration analyses of isotropic and composite plates using a linearly conforming radial point interpolation method. The present mesh-free shape functions were constructed by combining the radial and polynomial basis functions. A strain smoothing technique was introduced to the gradient matrix, and the discrete equilibrium equation and eigen equation were solved by performing nodal integration instead of Gauss integration. Numerical comparisons were made to validate the present formulation. The numerical examples have confirmed the significant features of the present method: (1) very stable and accurate for extremely distributed nodes; (2) shear-locking can be avoid very easily in the present formulation; (3) applicable for problems of complex domains.

References

[1] Liu GR. Meshfree methods: moving beyond the finite element method. New York: CRC Press; 2002.
[2] Gu YT. Meshfree method and their comparisons. Int J Comput Methods 2005;2:477–515.
[3] Naroles B, Touzot G, Villon P. Generalizing the finite element method: diffuse approximation and diffuse elements. Comput Mech 1992;10:307–18.
[4] Belytschko T, Lu Y, Gu L. Element-free Galerkin methods. Int J Numer Methods Eng 1994;37:229–56.
[5] Lucy LB. A numerical approach to the testing of the fission hypothesis. Astron J 1977;8:1013–24.
[6] Liu GR, Liu MB. Smoothed particle hydrodynamics: a meshfree particle method. New Jersey: World Scientific; 2003.
[7] Liu WK, Jun S, Zhang YF. Reproducing kernel particle methods. Int J Numer Methods Fluid 1995;20:1081–106.
[8] Atluri SN, Zhu T. A new meshless Petrov–Galerkin (MLPG) approach. Comput Mech 1998;22:117–27.
[9] Chen JK, Beraun JE, Jih CJ. Completeness of corrective smoothed particle method for linear elastodynamics. Comput Mech 1999;24:273–85.
[10] Batra RC, Zhang GM. Analysis of adiabatic shear bands in elasto-thermo-viscoplastic materials by modified smoothed-particle hydrodynamics (MSPH) method. J Comput Phys 2004;201:172–90.
[11] Liu GR, Gu YT. A point interpolation method for two-dimensional solids. Int J Numer Methods Eng 2001;50:937–51.
[12] Liu GR, Zhang GY, Dai KY, Wang YY, Zhong ZH, Li GY, et al. A linearly conforming point interpolation method (LC-PIM) for 2D solid mechanics problems. Int J Comput Methods 2006;2:645–65.

[13] Liu GR, Li Y, Dai KY, Luan MT, Xue W. A linearly conforming RPIM for solids mechanics problems. Int J Comput Methods 2006;3:401–28.
[14] Beissel S, Belytschko T. Nodal integration of the element-free Galerkin method. Comput Methods Appl Mech Eng 1996;139:49–74.
[15] Bonet J, Kulasegaram S. Correction and stabilization of smooth particle hydrodynamics methods with applications in metal forming simulation. Int J Numer Methods Eng 1999;47:1189–214.
[16] Chen JS, Wu CT, Yoon S, You Y. A stabilized conforming nodal integration for Galerkin mesh-free methods. Int J Numer Methods Eng 2001;50:435–66.
[17] Wang DD, Chen JS. Locking-free stabilized conforming nodal integration for meshfree Mindlin–Reissner plate formulation. Comput Methods Appl Mech Eng 2004;193:1065–83.
[18] Srinivas S, Rao AK. Bending, vibration and buckling of simply supported thick orthotropic rectangular plates and laminates. Int J Solids Struct 1970;6:1463–81.
[19] Srinivas S, Joga CV, Rao AK. An exact analysis for vibration of simply-supported homogeneous and laminated thick rectangular plates. J Sound Vibrat 1970;12:187–99.
[20] Pagano NJ. Exact solutions for rectangular bidirectional composites and sandwich plates. J Compos Mater 1970;4:20–34.
[21] Vel SS, Batra RC. Analytical solution for rectangular thick laminated plates subjected to arbitrary boundary conditions. AIAA J 1999;37:1464–73.
[22] Qian LF, Batra RC, Chen LM. Free and forced vibrations of thick rectangular plates using higher-order shear and normal deformable plate theory and Meshless Petrov–Galerkin (MLPG) method. Comput Model Eng Sci 2003;4:519–34.
[23] Ferreira AJM, Batra RC, Roque CMC, Qian LF, Martins PALS. Static analysis of functionally graded plates using third-order shear deformation theory and a meshless method. Compos Struct 2005;69:449–57.
[24] Hardy RL. Theory and applications of multiquadrics Bihamonics method (20 years of discovery 1968-1988). Comput Math Appl 1990;19:127–61.
[25] Hon YC, Lu MW, Xue WM, Zhu YM. Multiquadric method for the numerical solution of a biphasic mixture model. J Appl Math Comput 1997;88:153–75.
[26] Ferreira AJM, Roque CMC, Jorge RMN. Free vibration analysis of symmetric laminated composite plates by FSDT and radial basis functions. Comput Methods Appl Mech Eng 2005;194:4265–78.
[27] Ferreira AJM. Free vibration analysis of Timoshenko beams and Mindlin plates by radial basis functions. Int J Comput Methods 2005;2(1):15–31.
[28] Roque CMC, Ferreira AJM, Jorge RMN. Modelling of composite and sandwich plates by a trigonometric layerwise deformation theory and radial basis functions. Compos Part B - Eng 2005;36:559–72.
[29] Ferreira AJM, Batra RC, Roque CMC, Qian LF, Jorge RMN. Natural frequencies of functionally graded plates by a meshless method. Compos Struct 2006;75:593–600.
[30] Xiao JR, Batra RC, Gilhooley DF, Gillespie Jr JW, McCarthy MA. Analysis of thick plates by using a higher-order shear and normal deformable plate theory and MLPG method with radial basis functions. Comput Methods Appl Mech Eng 2007;196:979–87.
[31] Wang JG, Liu GR. A point interpolation meshless method based on radial basis functions. Int J Numer Methods Eng 2002;54:1623–48.
[32] Liu GR, Gu YT. A local radial interpolation method (LRPIM) for free vibration analysis of 2-D solids. J Sound Vibrat 2001;246:29–46.
[33] Wang JG, Liu GR, Lin P. Numerical analysis of Biot's consolidation process by radial point interpolation method. Int J Solids Struct 2002;39:1557–73.
[34] Liu GR, Dai KY, Lim KM, Gu YT. A radial point interpolation method for simulation of two-dimensional piezoelectric structures. Smart Mater Struct 2003;12:171–80.
[35] Dai KY, Liu GR, Lim KM, Chen XL. An element-free Galerkin method for static and free vibration analysis of shear-deformable laminated composite plates. J Sound Vibrat 2004;269:633–52.
[36] Dai KY, Liu GR, Han X, Lim KM. Thermomechanical analysis and active control of functionally graded material (FGM) plates using Element-free Galerkin method.. Comput Struct 2005;83:1487–502.
[37] Reddy JN. Mechanics of laminated composite plates and shells: theory and analysis. 2nd ed. CRC Press; 1996.
[38] Zienkiewicz OC, Taylor RL. The finite element method. Solid Mechanics, 5th ed., vol. 2. Butterworth-Heinemann; 2000.
[39] Timoshenko S, Woinowsky-Krieger S. Theory of plates and shells. New York: McGram-Hill; 1940.
[40] Khdeir AA, Reddy JN. Analytical solutions of refined plate theories of cross-ply composite laminates. J Pressure Vessel Technol 1991;113:570–8.
[41] Reddy JN, Miravete A. Practical analysis of composite laminates. Boca Raton (FL): CRC Press; 1995.
[42] Huang M, Sakiyama T. Free vibration analysis of rectangular plates with variously-shaped holes. J Sound Vibrat 1999;226:769–86.
[43] Ali R, Atwal SJ. Prediction of natural frequencies of vibration of rectangular plates with rectangular cutout. Comput Struct 1980;12:819–23.
[44] Belvins RD. Formulas for natural frequency and mode shape. New York: Springer; 1979.